

Alma Mater Studiorum Università di Bologna
Archivio istituzionale della ricerca

A Monolithic Cable-Driven Compliant Wrist for Prosthetic Arms

This is the final peer-reviewed author's accepted manuscript (postprint) of the following publication:

Published Version:

Baggetta M., Palli G., Melchiorri C., Berselli G. (2024). A Monolithic Cable-Driven Compliant Wrist for Prosthetic Arms. IEEE/ASME TRANSACTIONS ON MECHATRONICS, 29(2), 1052-1063 [10.1109/TMECH.2023.3345215].

Availability:

This version is available at: <https://hdl.handle.net/11585/971742> since: 2024-06-12

Published:

DOI: <http://doi.org/10.1109/TMECH.2023.3345215>

Terms of use:

Some rights reserved. The terms and conditions for the reuse of this version of the manuscript are specified in the publishing policy. For all terms of use and more information see the publisher's website.

This item was downloaded from IRIS Università di Bologna (<https://cris.unibo.it/>).
When citing, please refer to the published version.

(Article begins on next page)

A Monolithic Cable-Driven Compliant Wrist for Prosthetic Arms

Mario Baggetta *Member, IEEE*, Gianluca Palli *Member, IEEE*,
Claudio Melchiorri *Member, IEEE*, Giovanni Berselli *Member, IEEE*,

Abstract—This article presents a new design for a 2-Degrees Of Freedom compliant robotic wrist for upper limb prostheses that matches the maximum range of motion of a human wrist by utilizing Cross Axis Flexural Pivot (CAFP) as compliant joints. The wrist design is manufactured using additive manufacturing technology as a single, monolithic component. An optimization routine that utilizes the Bi-BCM technique to synthesize compliant joints in the wrist design is presented and verified using Finite Element Analysis (FEA). This optimization routine includes the computation of passive contact profiles through the centroid approach to prevent buckling in the CAFP compliant beams caused by external forces. Furthermore, an accurate analysis of various tendon routing paths for the actuation of the wrist is conducted, providing a flexible and reliable solution to avoid unnecessary power consumption. The proposed wrist is lightweight, cost-effective, easy to maintain, and thanks to the utilization of CAFP joints, it is frictionless and immune to backlash. Experimental tests are conducted to verify the FEA results and confirm the range of motion achieved by the joint (i.e., $\pm 80^\circ$ of Flexion/Extension, $\pm 40^\circ$ of Ulnar/Radial deviation). Overall, this paper demonstrates the development of a novel compliant robotic wrist that offers several advantages over traditional prostheses, including a wider range of motion, increased flexibility, and reduced maintenance costs.

Index Terms—Compliant Mechanisms, Monolith design, Additive Manufacturing, Prosthetic Wrist, CAFP.

I. INTRODUCTION

ROBOTIC wrist prostheses have been developed to address the limitations faced by upper limb amputees in performing daily activities. These prostheses aim to replicate the functions of the human wrist, which is a complex structure that provides essential degrees of freedom for manipulating objects. With the increasing number of individuals with upper limb amputations, there has been a growing interest in the design of prosthetic components by the scientific community in recent years.

The demand for upper limb prostheses is projected to increase significantly in the coming years, with over one million patients in the United States alone requiring an upper limb prosthesis by 2050 [1]. Moreover, wrist amputations account for a considerable proportion of upper limb amputations in

various countries, including Italy and the UK [2]. Hence, there is a pressing need to develop prosthetic wrist components that provide improved functionality to meet the needs of amputees.

The human wrist has three degrees of freedom (DOFs): flexion/extension (FE), ulnar/radial deviation (UR), and pronation/supination (PS). Although the latter DOF is carried out at the level of the forearm and is not typically considered in the design of prosthetic wrists, the first two DOFs are crucial for performing various tasks. Robotic wrists in the literature can be categorized as passive, body-powered, or active, depending on the mechanism used to generate the wrist movements [3].

Active robotic wrists, which are powered by electromechanical actuators, offer several advantages over passive or body-powered prostheses. However, their development has been limited by several factors, including their size, weight, number of DOFs, and range of motion (ROM). To achieve optimal functionality, the wrist component should be small enough to allow for the movement of power and sensor cables, as well as actuation tendons from the forearm to the hand, where the battery, motors, and controller are typically located. Furthermore, the weight of the wrist component should be minimized to reduce the overall power consumption of the prosthesis. Additionally, the number of DOFs and the attainable ROM of the wrist should be maximized to enable the performance of a broad range of daily activities.

While there have been numerous examples of robotic wrists reported in the literature (see [3] for an exhaustive review), few have achieved the desired combination of functionality and design. For example, Lee et al. [4] have designed a cable-driven compliant wrist, which reproduces the three rows of the human wrist based on the concept of tensegrity structure in order to realize a 1-DOF (i.e. FE) wrist with a range of motion of $[\pm 90^\circ]$. On the other hand, Demofonti et al. [5] have presented a 2-DOF compliant robotic wrist, of which the first (i.e. PS) is actively actuated within a range of $[\pm 90^\circ]$, while the second (i.e. FE) is a passive joint in a range of $[\pm 75^\circ]$, equipped with two levels of compliance (i.e. rigid state and compliant state). Following the same principle, Cappello et al. [6] have presented a quasi-passive joint capable of switching from a rigid to a relatively compliant configuration.

In order to obtain a wrist prosthesis that is as lightweight as possible but at the same time capable of a wide ROM, Kim et al. [7] have presented a contact-aided wrist composed of a two-row ellipsoid structure held together by passive teeth and always actuated through tendons. This 2-DOF wrist is able to have an FE range of $[\pm 80^\circ]$ and a UR range of $[\pm 25^\circ]$. Due to the fact that adding passive compliance to the

M. Baggetta, G. Berselli are with the Dept. of Mechanical, Energy, Management and Transportation Engineering, University of Genova, Genova, Italy.

G. Palli, C. Melchiorri are with the Dept. of Electrical Electronic and Information Engineering "Guglielmo Marconi", University of Bologna, Bologna, Italy.

G. Berselli is with the Dept. of Mechanical, Energy, Management and Transportation Engineering, University of Genova, Genova, Italy and with the Advanced Robotics Department (ADVR) at the Italian Institute of Technology

joint has been proven to be an effective way to ensure safety and robustness to component when interacting to human or unknown environment [8], Lee et al. have developed a robotic wrist with two-dimensional series elastic actuation to ensure an accurate Force/Torque interaction in the range of about $[\pm 50^\circ \text{ FE}, \pm 50^\circ \text{ UR}]$. Finally, Bilancia et al. [9] have presented a 2-DOF robotic wrist with the same stiffness and functional ROM as a human wrist using CAFPs elements and a series of active and passive contacts.

Despite these advancements, a robotic wrist that can match the maximum ROM of a human wrist (i.e. $[-76^\circ, +73^\circ]$ for the FE joint [10] and $[-25^\circ, +45^\circ]$ for the UR joint [11]) while being lightweight and compact enough to mimic its dimensions (i.e. approximately 43mm X 63mm for men [12] and 37mm X 56mm for women [13]) has not yet been developed. Furthermore, many of the previously introduced wrists consist of numerous components, making them challenging to assemble and maintain.

To address these issues, this paper proposes a novel 2-DOF compliant robotic wrist for upper limb prostheses. Taking into account the existing literature and the aforementioned considerations, the proposed wrist can match the maximum ROM of the human wrist's FE and UR deviation joints, while being produced using additive manufacturing technology as a single, monolithic component. The resulting wrist is lightweight, cost-effective, easy to maintain, and equipped with CAFPs compliant joints for each of the wrist's DOFs, which are free from friction and backlash issues. Overall, the novel contributions of the present paper can be listed as follows:

- Design and development of an innovative robotic wrist, providing the desired combination of functionality, limited dimensions and ease-of-use for application in upper limb prosthetic;
- The introduction of a fast and precise optimization algorithm for synthesizing CAFP joints, purposely tailored to wrist design. This optimization algorithm employs the Bi-BCM technique and includes the generation of passive contact profiles to guide the wrist deflection and prevent buckling issues arising from external forces [9].
- Detailed Finite Element Analysis (FEA) simulations to evaluate different tendon routing techniques for wrist remote actuation, aiming at the determination of the most energy-efficient routing method.

The remainder of this article is structured as follows: Section 2 describes the design and optimization of the CAFP joints used to create the wrist, Section 3 presents the final design that includes the design of passive contacts, Section 4 presents the virtual prototype of the wrist and the respective results obtained, Section 5 describes the physical prototype and the tests conducted on it, and finally, Section 6 provides the conclusions of this research work.

II. WRIST DESIGN AND OPTIMIZATION

The proposed robotic wrist employs CAFP joints [14], [15] to enable its two degrees of freedom. This particular compliant mechanism (CM) [16] is of common use in precision mechanics, aeronautics, robotics, and prosthetics [9], [17]–[20].

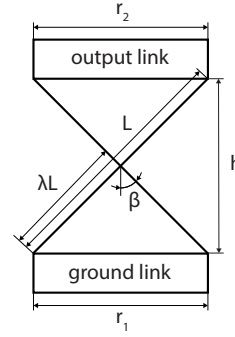


Fig. 1: CAFP characteristic variables.

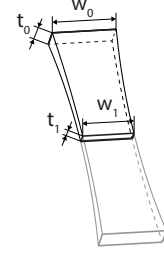


Fig. 2: CAFP beam profile.

It possesses all the advantages of CM, such as the possibility to be designed as a compact monolithic component that is free of friction, backlash, and the need for lubrication. Moreover, it is one of the wider deflection 1-DOF compliant joints. Referring to Figure 1, it consists of two rigid links, a ground link that is fixed, and an output link that is free to move, connected to each other by two cross-shaped slender beams with a rectangular cross-section. The CAFP's characteristic geometric parameters are the semi-angle between the beams β and the position where the beams intersect, which is determined by the parameter λ . The other parameters shown in the figure are the ground link width r_1 , the output link width r_2 , and the beam length L . One of these parameters (e.g. r_1) can be taken as an independent variable, along with β and λ , to obtain the other parameters as follows:

$$r_2 = r_1 * \frac{1 - \lambda}{\lambda}; \quad h = \frac{r_1 + r_2}{2 * \tan(\beta)}; \quad L = \frac{r_1}{2 * \lambda * \sin(\beta)} \quad (1)$$

Despite its numerous advantages, designing and optimizing the CAFP presents challenges. This is primarily due to its distinctive characteristic of having a marked center shift, where the center of rotation is not fixed during deflection, and its high sensitivity to variations in its parameters. Various methods have been employed to investigate the CAFP. These methods include the use of the Beam Constraint Model (BCM) equations [21] and the Chained-Beam Constraint Model (CBCM) [22]. The CBCM, in particular, involves linking multiple BCM elements in series to extend the limited rotation range of the original BCM. However, when variable-section beams, as shown in Figure 2, are utilized, neither of these methods remains applicable, necessitating the use of Finite Element Analysis (FEA). FEA, while powerful, is a more complex tool that requires significantly more computational time compared to BCM and CBCM. A comprehensive exploration of various techniques and tools for designing compliant elements like the CAFP can be found in [23].

In our previous work [24], we introduced a novel theoretical approach known as Bi-BCM to address the current limitations associated with CAFP (Compliant Adaptive Flexure Pivot) analysis. Bi-BCM employs two BCM (Beam Constraint Model) elements and is designed to comprehensively analyze CAFP systems with beams featuring variable cross-sections, both in terms of thickness and width. This approach allows

for rapid and precise evaluation of CAFP mechanisms within a rotation range of up to 50 degrees, with a maximum error of less than 5%. We specifically chose variable section beams, as illustrated in Figure 2, for our study. These beams have been demonstrated to effectively reduce stress on the beam itself, leading to an increased maximum deformation. Additionally, they help minimize the variation of the joint's instantaneous rotation center, also known as the center shift.

In this paper, the Bi-BCM technique have been utilized in conjunction with a Matlab optimization routine to analyze the CAFP mechanism incorporated within the proposed wrist design. The ability to create beams with variable cross-sections plays a pivotal role in minimizing the prototype's dimensions while ensuring that it remains within the material's yield limits.

A. Bi-BCM Optimization Routine

This subsection introduces the optimization routine used to design compliant wrist joints, which is based on the CAFP solution theory known as the Bi-BCM, as documented in [24]. To maintain brevity, we won't delve into the intricate details of the solution theory. Instead, our focus is on outlining the

primary steps and implementation for the presented case study. Figure 3 illustrates the flowchart of the optimization procedure approach.

The first step involves selecting the design variables for our case study, which include r_1 , w_0 , w_1 , t_0 , and t_1 . These variables should be distinguished from other parameters, such as r_2 , β , λ , h , L , L_{el1} , L_{el2} and the flexural Young's modulus of the material, denoted as E . L_{el1} and L_{el2} represent the lengths of the two beam sections, which, with $\lambda=0.5$, are equivalent to $L/2$. The value of E has been fixed at 1400 MPa, taking into account the material properties of Nylon 11 powder, which is compatible with the Formlabs Fuse printing process. Additionally, r_2 , h , and L have been calculated according to Equation 1, while λ and β have been assigned values of 0.5 and 70° , respectively. The value of λ ensures that the initial center of rotation of the CAFP, located at the intersection of the beams, corresponds to its center of mass. β has been chosen as the maximum feasible value while avoiding contact between the beam and the links at the maximum deflection of $\theta_{max} = 40^\circ$. The value of θ_{max} has been set equal to 40° to achieve the required deflection of the Ulnar/Radial DOF using a single CAFP module and the required deflection of the Flexion/Extension module (i.e. 80°) using two CAFP modules connected in series. This choice has been made because the accuracy of the Bi-BCM mathematical model is ensured for rotations up to 50 degrees, making it impossible to achieve an 80-degree rotation with a single component using this technique. Moreover, the practice of connecting multiple modules in series to increase joint deflection has been extensively and effectively applied in the field of reconfigurable robots. This approach has been exemplified by works like the ones reported by Kaufmann et al. [25] and Chen et al. [26], who have demonstrated the benefits of this solution.

Using Matlab software, a multi-objective optimization has been implemented with the aim of minimizing the CAFP size without necessarily sacrificing its stiffness. Specifically, for each optimization iteration, a total of 10 simulation steps have been set (e.g., every 4° of deflection), with a maximum allowable stress σ_s for accepting the solution specified as 35 MPa out of a material's maximum allowable stress of 55 MPa. The choice of 10 simulation steps has been made to achieve an almost perfect match between FEM and Bi-BCM. Increasing the step count beyond this point only results in higher computational costs without clear advantages. Due to the high number of design variables, a genetic algorithm (*ga*) has been chosen over the well-known *fmincon* algorithm to avoid relative minima of the objective functions. The height h and the reciprocal of the reaction torque $1/M_r$ of the CAFP have been selected as objective functions based on the above considerations. To summarize, the design optimization problem can be formulated as follows:

$$\text{minimize } \left(h = \frac{r_1 + r_2}{2 * \tan(\beta)}, \frac{1}{M_r} \right)$$

$$\text{with respect to } \Delta = [r_1, \omega_0, \omega_1, t_0, t_1]$$

$$\text{subject to } \sigma(\theta_{max}) < \sigma_s; \Delta \in [\Delta_{min}, \Delta_{max}]$$

In this study, the shape of the beam has been adjusted by

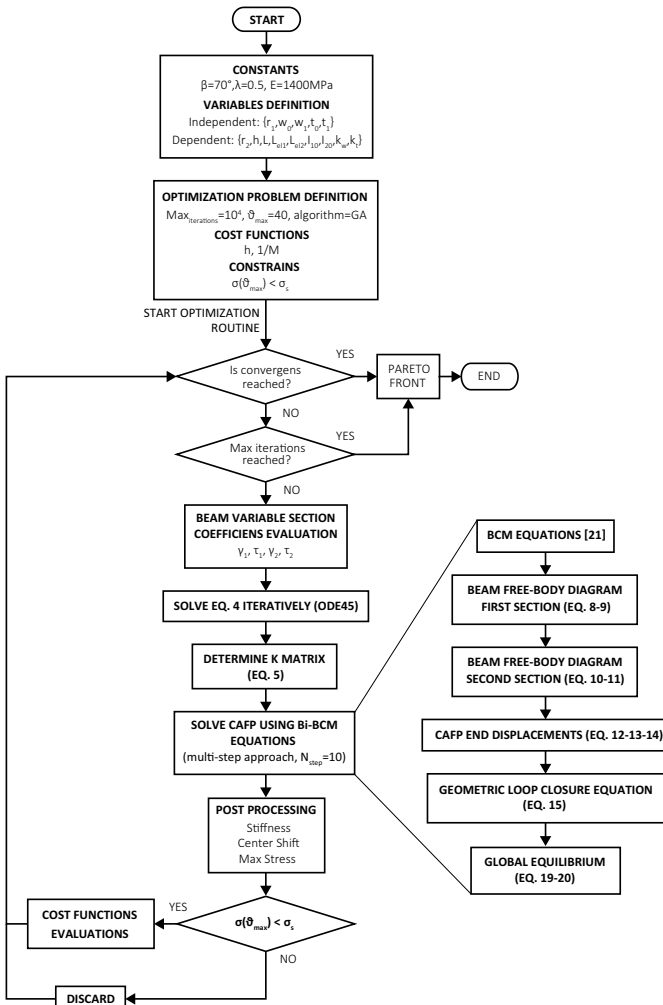


Fig. 3: Flowchart of the optimization approach.

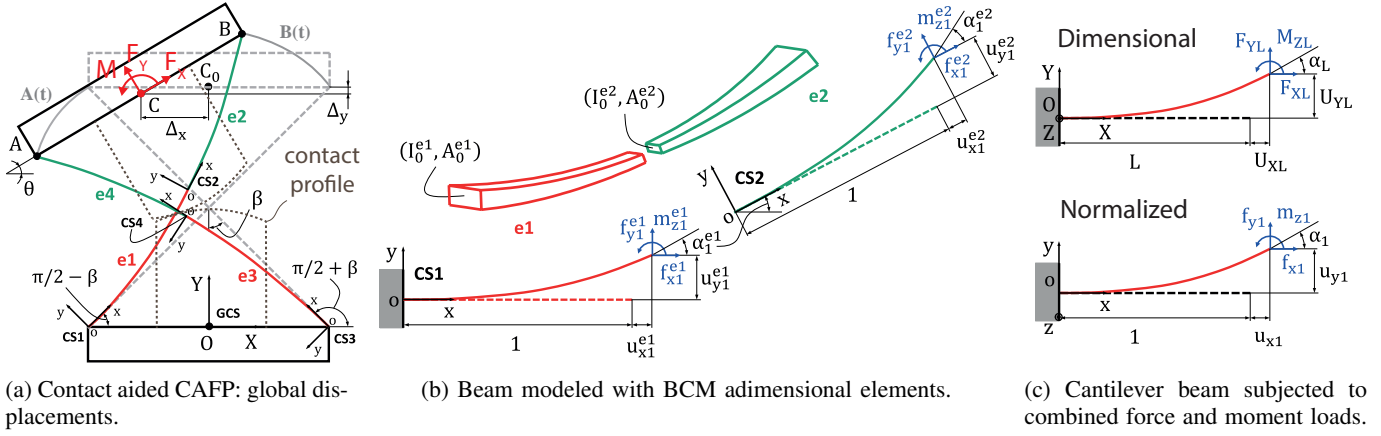


Fig. 4: Bi-BCM CAFP model.

varying both its width and thickness through the application of second-order (parabolic) laws. This choice is based on their demonstrated superior effectiveness in stress control compared to first-order (linear) laws, as shown in [24]. The equations for the variable section beam can be formulated as follows:

$$w(x) = w_0(1 + \gamma_1 x + \gamma_2 x^2) \quad (2)$$

$$t(x) = t_0(1 + \tau_1 x + \tau_2 x^2) \quad (3)$$

$$A(x) = w_0 t_0 (1 + \gamma_1 x + \gamma_2 x^2)(1 + \tau_1 x + \tau_2 x^2) = A_0 \eta(x)$$

$$I(x) = \frac{w_0 t_0^3}{12} (1 + \gamma_1 x + \gamma_2 x^2)(1 + \tau_1 x + \tau_2 x^2)^3 = I_0 \xi(x)$$

where γ_1 , γ_2 , τ_1 and τ_2 are the beam's section shape coefficients, w_0 and t_0 are the initial beam width and thickness, respectively, $A_0 = w_0 t_0$, $I_0 = \frac{w_0 t_0^3}{12}$, η and ξ are characteristic functions of the variable section beam. The optimization routine begins by calculating the BCM coefficients, denoted as k_{ab}^n following the same nomenclature used in the work by Awatar et al. [21], which has presented solutions for uniform section beam flexures. It is crucial to note that the BCM coefficients strictly depend on the beam's shape (not its size). In other words, they have to be adjusted every time modifications are made to the characteristic functions of the variable section beam η and ξ . By considering each beam of the CAFP as two BCM elements as shown in Figure 4.b and defining the width coefficient $k_w = w_1/w_0$ and the thickness coefficient $k_t = t_1/t_0$, for the first beam element $k_w, k_t < 1$, which gives:

$$\gamma_1 = -2\gamma_2 \quad \tau_1 = -2\tau_2 \quad \gamma_2 = 1 - k_w \quad \tau_2 = 1 - k_t$$

while, for the second element, $k_w, k_t > 1$, which instead gives:

$$\gamma_1 = 0 \quad \tau_1 = 0 \quad \gamma_2 = k_w - 1 \quad \tau_2 = k_t - 1$$

When considering a CAFP that is subjected to a load set consisting of a combined moment M and forces F_X and F_Y acting on the output link following the schematic in Figure 4.c and assuming that $I(x) = I_0 \xi(x)$ where $I(0) = I_0$, the normalized following BCM governing equations can be applied [24]:

$$u_y''(x) = \frac{m_{z1} + f_{y1}(1-x) - f_{x1}(u_{y1} - u_y(x))}{\xi(x)} \quad (4)$$

$$u_y(0) = 0, u_y'(0) = 0$$

where the problem has been adimensionalized with respect to the beam length L , u_{y1} is the end planar displacement of the beam with respect to y , $u_y(x)$ is the beam y -displacement function, m_z , f_y , and f_x as the end loads applied on the beam after adimensionalization. Equation 4 can be solved using numerical techniques in Matlab, specifically employing the *ODE45* solver. The algorithm takes inputs such as f_{x1} , f_{y1} , m_{z1} , and $\xi(x)$, and yields $u_y(x)$ along with its derivative as output. However, since u_{y1} is initially unknown, an iterative approach is necessary to obtain accurate results. In practice, the numerical value of the prescribed vertical displacement at the end, denoted as u_{y1}^i at the i -th iteration step, is compared with the corresponding value obtained from the solution of Eq. 4 at $x = 1$ to determine the updated input value for the $(i+1)$ -th iteration, which is given by $u_{y1}^{i+1} = u_{y1}^i + \varphi(u_y(1) - u_{y1}^i)$, where φ is a parameter defined by the user. Convergence of the algorithm is achieved when the computed error between these two values is less than a specified tolerance, denoted as ϵ . To ensure accurate and efficient results, suitable values for φ and ϵ are typically chosen, for example, as 0.1 and 10^{-5} , respectively. To compute the BCM coefficients for a specified beam shape, as defined in Equation 4 using the function $\xi(x)$, it is necessary to calculate the beam stiffness matrix. This matrix is determined at discrete points within the range of f_{x1} values spanning from -0.5 to 0.5.

$$K(\xi, f_{x1}) = \begin{bmatrix} k_{11}(\xi, f_{x1}) & k_{12}(\xi, f_{x1}) \\ k_{21}(\xi, f_{x1}) & k_{22}(\xi, f_{x1}) \end{bmatrix} \quad (5)$$

However, since it is not directly available, it can be obtained by solving and inverting the compliance matrix C .

$$\begin{bmatrix} u_{y1} \\ \alpha_1 \end{bmatrix} = \begin{bmatrix} c_{11}(\xi, f_{x1}) & c_{12}(\xi, f_{x1}) \\ c_{21}(\xi, f_{x1}) & c_{22}(\xi, f_{x1}) \end{bmatrix} \begin{bmatrix} f_{y1} \\ m_{z1} \end{bmatrix} \quad (6)$$

Indeed, when $f_{y1} = 0.5$ and $m_{z1} = 0$, we obtain the end displacement u_{y1} and rotation $\alpha_1 = u_y'(1)$, which provide the terms c_{11} and c_{21} for a specific value of f_{x1} . Similarly, when $f_{y1} = 0$ and $m_{z1} = 0.5$, we acquire the terms c_{12} and c_{22} . The matrix K is subsequently determined by performing the inversion of C . After this iterative process for various values of

f_{x1} , we can employ a polynomial fitting technique to analyze the collected data and establish the following relationships:

$$\begin{aligned} k_{11}(\xi, f_{x1}) &= k_{11}^{(0)} + f_{x1}k_{11}^{(1)} + f_{x1}^2k_{11}^{(2)} + \dots \\ k_{12}(\xi, f_{x1}) &= k_{12}^{(0)} + f_{x1}k_{12}^{(1)} + f_{x1}^2k_{12}^{(2)} + \dots \\ k_{22}(\xi, f_{x1}) &= k_{22}^{(0)} + f_{x1}k_{22}^{(1)} + f_{x1}^2k_{22}^{(2)} + \dots \end{aligned} \quad (7)$$

from which the BCM stiffness coefficients k_{ab}^n are easily extrapolated, noting that $k_{12}^{(n)} = k_{21}^{(n)}$ on the basis of Maxwell's reciprocity. Once the coefficient of the variable beam have been calculated, the Bi-BCM equations can be employed to solve the CAFB and obtain the objective functions values. Referring to Figure 4.b, in order to ensure the proper load distribution between the two beam elements, it is essential to maintain the local static equilibrium. Upon examining the free-body diagram, the following equations for the first beam section can be written:

$$\begin{bmatrix} f_{x1}^{e1} \\ f_{y1}^{e1} \end{bmatrix} \Psi_0^{e1} - \begin{bmatrix} \cos(\alpha_1^{e1}) & -\sin(\alpha_1^{e1}) \\ \sin(\alpha_1^{e1}) & \cos(\alpha_1^{e1}) \end{bmatrix} \begin{bmatrix} f_{x1}^{e2} \\ f_{y1}^{e2} \end{bmatrix} \Psi_0^{e2} = 0 \quad (8)$$

$$m_{z1}^{e1} \Psi_0^{e1} L_{e1} - [m_{z1}^{e2} + (1 + u_{x1}^{e2}) f_{y1}^{e2} - u_{y1}^{e2} f_{x1}^{e2}] \Psi_0^{e2} L_{e2} = 0 \quad (9)$$

and, for the second CAFB's beam, these become:

$$\begin{bmatrix} f_{x1}^{e3} \\ f_{y1}^{e3} \end{bmatrix} \Psi_0^{e3} - \begin{bmatrix} \cos(\alpha_1^{e3}) & -\sin(\alpha_1^{e3}) \\ \sin(\alpha_1^{e3}) & \cos(\alpha_1^{e3}) \end{bmatrix} \begin{bmatrix} f_{x1}^{e4} \\ f_{y1}^{e4} \end{bmatrix} \Psi_0^{e4} = 0 \quad (10)$$

$$m_{z1}^{e3} \Psi_0^{e3} L_{e3} - [m_{z1}^{e4} + (1 + u_{x1}^{e4}) f_{y1}^{e4} - u_{y1}^{e4} f_{x1}^{e4}] \Psi_0^{e4} L_{e4} = 0 \quad (11)$$

where $\Psi_0^e = EI_0^e/L_e^2$ (with $e = e_1, e_2, e_3, e_4$). Subsequently, for both of the pivot beams, the following expressions provide the dimensional end displacements at points A and B in the context of coordinate systems CS1 and CS3, as depicted in Fig. 4.a:

$$\begin{aligned} \begin{bmatrix} U_{XA} \\ U_{YA} \end{bmatrix} &= \begin{bmatrix} \cos(\alpha_1^{e3}) & -\sin(\alpha_1^{e3}) \\ \sin(\alpha_1^{e3}) & \cos(\alpha_1^{e3}) \end{bmatrix} \begin{bmatrix} L_{e4}(1 + u_{x1}^{e4}) \\ L_{e4}u_{y1}^{e4} \end{bmatrix} \\ &+ \begin{bmatrix} L_{e3}(1 + u_{x1}^{e3}) \\ L_{e3}u_{y1}^{e3} \end{bmatrix} \end{aligned} \quad (12)$$

$$\begin{aligned} \begin{bmatrix} U_{XB} \\ U_{YB} \end{bmatrix} &= \begin{bmatrix} \cos(\alpha_1^{e1}) & -\sin(\alpha_1^{e1}) \\ \sin(\alpha_1^{e1}) & \cos(\alpha_1^{e1}) \end{bmatrix} \begin{bmatrix} L_{e2}(1 + u_{x1}^{e2}) \\ L_{e2}u_{y1}^{e2} \end{bmatrix} \\ &+ \begin{bmatrix} L_{e1}(1 + u_{x1}^{e1}) \\ L_{e1}u_{y1}^{e1} \end{bmatrix} \end{aligned} \quad (13)$$

$$\alpha_1^{e1} + \alpha_1^{e2} = \alpha_1^{e3} + \alpha_1^{e4} = \theta \quad (14)$$

Equation 14 is a result of the fixed connection between the beams and the output link. When a vectorial rotations of $(\pi/2 - \beta)$ and $(\pi/2 + \beta)$ is applied, corresponding to the orientation angles of CS1 and CS3 (see Fig. 4.a), to the quantities expressed in Eqs. 12 and 13, the overall geometric loop closure can be written as:

$$\begin{aligned} &\begin{bmatrix} \sin(\beta) & -\cos(\beta) \\ \cos(\beta) & \sin(\beta) \end{bmatrix} \begin{bmatrix} U_{XB} \\ U_{YB} \end{bmatrix} - \begin{bmatrix} -\sin(\beta) & -\cos(\beta) \\ \cos(\beta) & -\sin(\beta) \end{bmatrix} \\ &\times \begin{bmatrix} U_{XA} \\ U_{YA} \end{bmatrix} - \begin{bmatrix} r_1 + r_2 \cos(\theta) \\ r_2 \sin(\theta) \end{bmatrix} = \begin{bmatrix} 0 \\ 0 \end{bmatrix} \end{aligned} \quad (15)$$

The output link displacements, Δ_X and Δ_Y , are then given by:

$$\Delta_X = \frac{X_A + X_B}{2} \quad \Delta_Y = \frac{Y_A + Y_B}{2} - h \quad (16)$$

$$\begin{bmatrix} X_A \\ Y_A \end{bmatrix} = \begin{bmatrix} -\sin(\beta) & -\cos(\beta) \\ \cos(\beta) & -\sin(\beta) \end{bmatrix} \begin{bmatrix} U_{XA} \\ U_{YA} \end{bmatrix} + \begin{bmatrix} r_1/2 \\ 0 \end{bmatrix} \quad (17)$$

$$\begin{bmatrix} X_B \\ Y_B \end{bmatrix} = \begin{bmatrix} \sin(\beta) & -\cos(\beta) \\ \cos(\beta) & \sin(\beta) \end{bmatrix} \begin{bmatrix} U_{XB} \\ U_{YB} \end{bmatrix} - \begin{bmatrix} r_1/2 \\ 0 \end{bmatrix} \quad (18)$$

where $[U_{XA}, U_{YA}]$ and $[U_{XB}, U_{YB}]$ are the end planar displacement of points A and B, respectively. To complete the Bi-BCM model, the global equilibrium equations must be defined by taking into consideration all the forces and moments acting on the output link, as depicted in Fig. 4.a:

$$\begin{aligned} \begin{bmatrix} F_x \\ F_y \end{bmatrix} &= \Psi_0^{e1} \begin{bmatrix} \sin(\beta) & -\cos(\beta) \\ \cos(\beta) & \sin(\beta) \end{bmatrix} \begin{bmatrix} f_{x1}^{e1} \\ f_{y1}^{e1} \end{bmatrix} \\ &+ \Psi_0^{e3} \begin{bmatrix} -\sin(\beta) & -\cos(\beta) \\ \cos(\beta) & -\sin(\beta) \end{bmatrix} \begin{bmatrix} f_{x1}^{e3} \\ f_{y1}^{e3} \end{bmatrix} \end{aligned} \quad (19)$$

$$M = \Psi_0^{e3} r_2 [\sin(\theta) \quad -\cos(\theta)] \begin{bmatrix} -\sin(\beta) & -\cos(\beta) \\ \cos(\beta) & -\sin(\beta) \end{bmatrix} \begin{bmatrix} f_{x1}^{e3} \\ f_{y1}^{e3} \end{bmatrix} \quad (20)$$

$$- \frac{r_2}{2} [\sin(\theta) \quad -\cos(\theta)] \begin{bmatrix} F_x \\ F_y \end{bmatrix} + m_{z1}^{e2} \Psi_0^{e2} L_{e2} + m_{z1}^{e4} \Psi_0^{e4} L_{e4}$$

Furthermore, the Bi-BCM equations provide the stiffness function $K_M = \frac{\partial M}{\partial \theta}$ and the beam's normal stress $\sigma(x) = \sigma_b(x) + \sigma_a$, where $\sigma_b(x)$ is the bending stress along the element's x-axis, and σ_a is the tensile stress due to the axial force. The bending stress is given by:

$$\sigma_b(x) = \frac{6M_b(x)}{w(x)t(x)^2} \quad (21)$$

where $M_b(x)$ is the local bending moment function. The tensile stress can be calculated using the following equation:

$$\sigma_a = \frac{f_{x1}EI_0/L_e^2}{w(x)t(x)} \quad (22)$$

Once the optimizer converges or the maximum number of iterations is reached, the optimization terminates. Notably, each simulation takes approximately 0.6 seconds on an Intel(R) Core(TM) CPU @ 2.5 GHz and 16 GB RAM workstation, compared to the 480 seconds required to solve the same model through FEA analysis with at least three rows of elements along the beams' thickness.

B. Optimization Results

Table I presents a summary of the selected intervals for the design variables and their respective optimal values for the two wrist modules (FE and UR). The objective function values obtained as output of the optimization routine, which are the same for both modules, are as follows: $H = 7.321$ mm and $M_r = 83.201$ Nmm for the FE module and $H = 8.251$ mm and $M_r = 83.648$ Nmm for the UR module. It should be noted that the first degree of freedom to be optimized corresponds

TABLE I: Optimal values of the CAFPs. "optimization range and optimal values"

Flexion/Extension module		
Design Var.	Range	Opt. Value
r_1	[15,25] mm	20.114 mm
w_0	[5,10] mm	9.159 mm
w_1	[5,10] mm	8.593 mm
t_0	[0.5,1.5] mm	1.018 mm
t_1	[0.5,1.5] mm	0.938 mm
Ulnar/Radial module		
Design Var.	Range	Opt. Value
r_1	[20,30] mm	22.669 mm
w_0	[5,10] mm	7.178 mm
w_1	[5,10] mm	6.767 mm
t_0	[0.5,1.5] mm	1.131 mm
t_1	[0.5,1.5] mm	1.061 mm

to the FE joint of the wrist. This joint contributes significantly to the overall size of the wrist, as two modules are required to achieve full deflection of the joint while maintaining a smaller width with respect to the UR module. To simplify the design, the wrist was modeled with an elliptical cross-section, with maximum dimensions of 30 mm by 40 mm, which is consistent with the human counterpart.

To evaluate the impact of the CAFP geometry on the results, Figure 5 displays the Pareto front associated with the FE module and the corresponding references of the 3D component. The middle component was chosen as the optimal design since it is the result just before the left asymptote, where the height of the component stops decreasing in favor of the decrease of the joint reaction force alone.

Regarding the wrist UR module, the Figure 6 depicts only the Pareto front, with the optimal value highlighted in red. In this particular case, the decision has been made to select the point with the same reaction torque obtained from the FE module, rather than the one providing the smallest height. This approach take into consideration the use of two FE modules capable of supporting rotations up to 40 degrees, which are necessary to achieve the required angular rotation of the FE module (i.e., 80 degrees). As a result, a UR module with twice the stiffness of the FE module will be obtained, emulating the natural difference in stiffness present in the human wrist [27]. The effectiveness and accuracy of the Bi-BCM technique compared to FEA analysis is demonstrated in Figure 7 by presenting the torque/deflection graphs of the two optimized modules. The maximum errors for the FE module and UR module were found to be less than 4% and 3%, respectively. The FEA analysis employed Hexa8 elements with a maximum element size of 0.15mm and a total of 16083 elements, using the commercial software package Recurdyn.

III. FINAL DESIGN OF THE WRIST

After optimizing each of the two compliant wrist modules, they need to be combined to create the final design that meets the required 2 DOF. Figure 8 depicts the design procedure used to propose two distinct wrist designs. The first design, referred to as the "universal joint configuration," aims to mimic a spherical joint by assembling the two FE modules at the component ends, separated by the UR module. This configuration enables both the DOF of the wrist to rotate about

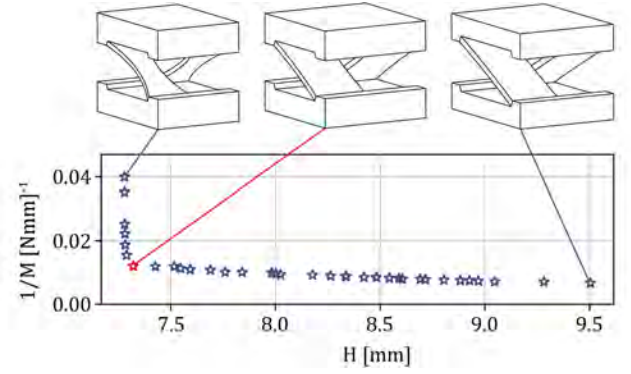


Fig. 5: Plot and graphical representation of the Pareto frontier for the Flexion/Extension module.

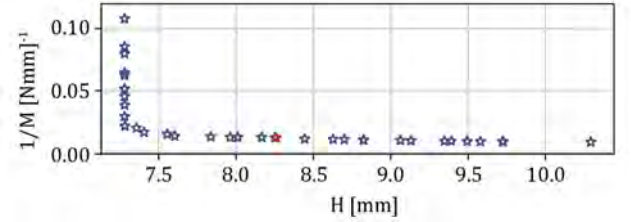


Fig. 6: Plot of the Pareto frontier for the Ulnar/Radial module.

the device's center of rotation, except for any shifts caused by the CAFP during deflection.

The second design, chosen by the authors for further development, involves assembling the two FE modules in series. This configuration results in the centers of instantaneous rotation of the FE and UR wrist modules being misaligned from each other. By splitting the two modules into separate hinge joints, this design allows for more narrow hand movements, as illustrated in Figure 9.

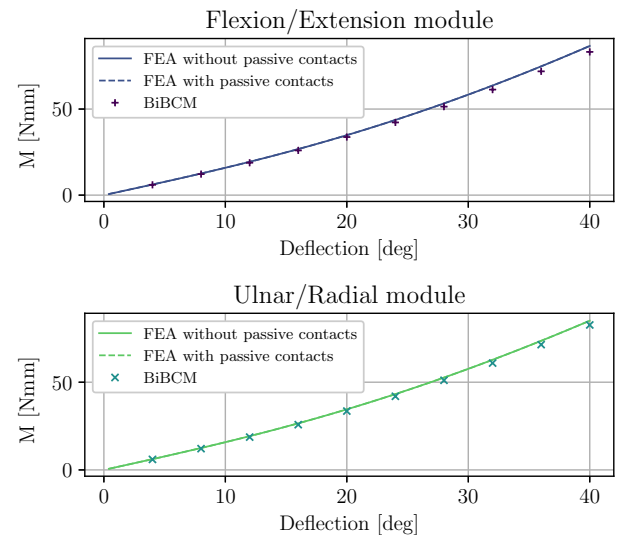


Fig. 7: Reaction forces of the proposed wrist with the maximum allowed deflections, comparison between the FEA and BiBCM.

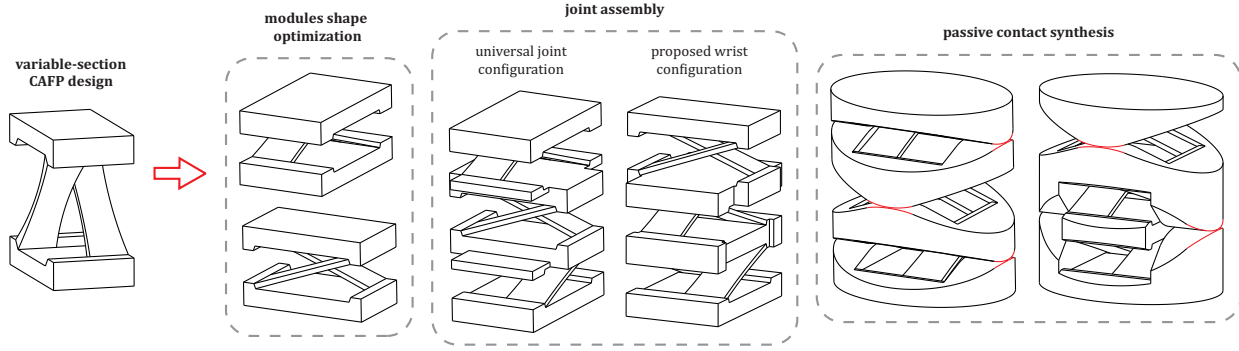


Fig. 8: Compliant wrist design procedure.

A. Passive contacts

One problem with the CAFP is its vulnerability to external loads or impacts, which could cause the beams to buckle. To address this issue in the final prototype, passive contacts have been designed to support the joint and protect the beams from unexpected loads, as depicted in Figure 8. Unlike a simple hinge, the CAFP lacks a single center of instantaneous rotation and tends to move during joint deflection. Therefore, the pure rolling contact design necessitates the centroids approach [9]. As explained in Subsection II-A, the Bi-BCM outputs include the planar displacements of the two points A and B of the mobile link of the CAFP, along with their derivatives. These outcomes allow for the determination of the centroid of the CAFP at each time step with respect to the fixed reference system by intersecting the orthogonal vectors to the velocities $v_A(t)$ and $v_B(t)$ for each point on the trajectories $A(t)$ and $B(t)$ (Figure 4.a). Using a simple coordinate transformation, the position of the centroid relative to the mobile reference system can then be determined. Finally, the two centroid trajectories, depicted in red in Figure 8, are imported into the CAD software to complete the wrist design.

To better summarize the proposed wrist's features, a comparison with currently commercialized or literature-present prosthetic wrist models is provided in Table II, demonstrating that it is lighter and smaller than the majority of them while providing a higher ROM.

IV. FEA ANALYSIS

The final prototype of the wrist underwent FEA analysis using Recurdyn software. The model consisted of 60311 *Hexa8*

TABLE II: Prosthetic Wrists Properties.

Model	Size [mm]	Weight [g]	ROM [°]
Proposed Wrist	30*40*40	20	± 80 FE, ± 40 UR
i-Limb	49* $\phi 50$	161	± 40 FE, 0 UR
Be-Bionics	25* $\phi 50$	141	± 30 FE, ± 30 UR
Lee et al. [4]	29*43*37	20	± 90 FE, 0 UR
Demofonti et al. [5]	40* $\phi 48$	65	± 75 FE, 0 UR
Kim et al. [7]	30*50*30	30	± 80 FE, ± 25 UR

elements, with a maximum element size of 0.15 mm near the beams and 0.5 mm for the remaining parts. The dimensions of each module are listed in Table I, while the overall dimensions of the wrist are 30x40x40(H) mm with an elliptical cross-section. Nylon 11 has been chosen as the material for its high strength-to-weight ratio and ease of printability. During the FEA simulations, the bottom of the ground link has been constrained with a zero displacement boundary condition, while an angular displacement equal to θ_{max} has been applied at a master node rigidly connected to the upper surface of the output link. Additionally, *GeoSurface* contacts have been included to simulate the joint's passive contacts behavior. Figure 9 displays contour plots of the two configurations presented (i.e., the one proposed by the authors in Figures #1 and #3 and the one mimicking a universal joint in Figures #2 and #4). The maximum stress was consistent with the one calculated using the Bi-BCM equations (lower or equal to 35 MPa), as were the torque values during deflection, as shown in Figure 10. Furthermore, the passive contacts during rotation never came into operation, confirming the correct computation of the joint's pure rolling profile. The two wrist modules reach the same maximum torque (i.e., approximately 83 Nmm), and

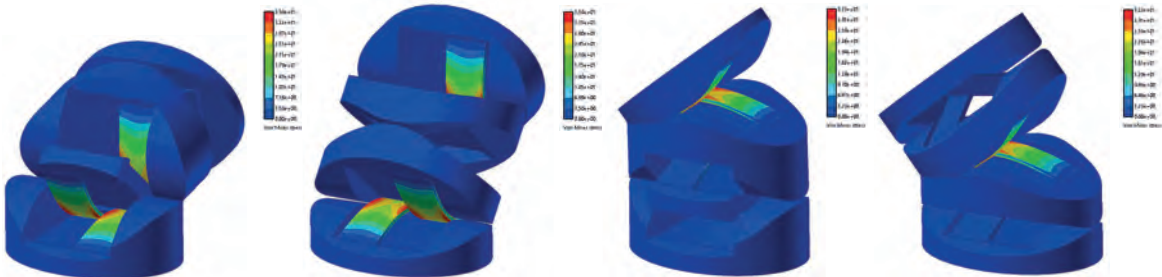


Fig. 9: FEA analysis of the series (figures #1 and #3) and universal joint (figures #2 and #4) versions of the proposed prosthetic wrist.

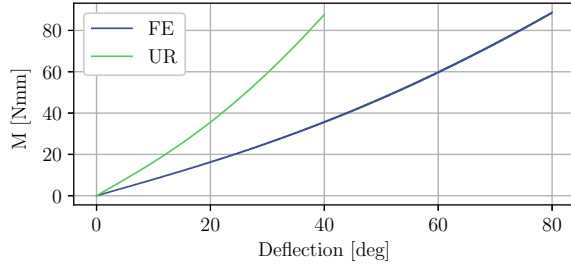


Fig. 10: Maximum allowed deflections for the FE and UR modules in the proposed wrist, along with the corresponding reaction forces.

therefore, given the halved deflection, the UR module has double the stiffness compared to the FE module. Notably, the optimization routine presented in this paper allows for complete customization of every characteristic of the CAFP joint based on application requirements.

A. Tendons Path

Assuming that forces stay significantly below the tendon's maximum load, simulating tendons becomes a straightforward process achieved by applying axial forces at attachment points, ensuring fast and efficient simulations. In contrast, alternative approaches, such as utilizing rigid elements with elastic springs or conducting finite element analysis on the tendon (using 'solid' or 'beam' elements) [28], present computational challenges and maintain a level of imprecision. The placement of tendons in objects with cylindrical shapes and one or more degrees of freedom usually involves two configurations: one with tendons located at the ends, forming a "plus" shape, and one with tendons located at the corners, forming a "cross" shape. Figure 11 illustrates these configurations. Assuming four linear motors (e.g., electromechanical, twisted cable, or artificial pneumatic muscles as those implemented in [7]) are used, the "plus" configuration connects a single motor with its motion law to each tendon, hence allowing for control of each possible joint movement, such as flexion, extension, ulnar

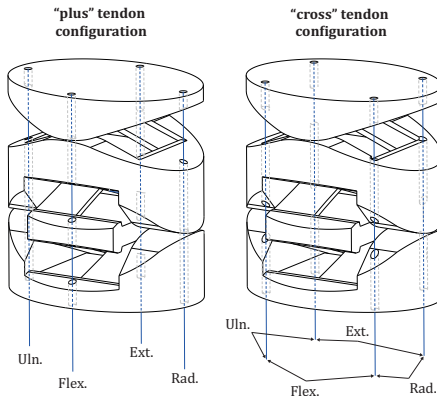


Fig. 11: Compliant wrist: "plus" and "cross" tendon configurations.

deviation, and radial deviation. In contrast, in the "cross" configuration, all four motors are involved in any wrist deflection, making their control more complex. In our specific geometry, using the "cross" configuration results in a more energy-intensive actuation of the device, a crucial consideration in prosthetic design where limited battery space is a concern. As depicted in Figure 12, the work done by motors (calculated as the force multiplied by the tendon displacement) in the "cross" configuration is 658% higher for the FE deflection and 42% higher for the UR deflection compared to the "plus" configuration. This increase is primarily due to the less favorable position of tendons in the "cross" configuration, resulting in minimal leverage near maximum deflections. Considering all these factors, the "plus" configuration stands as the preferred choice for implementing in the proposed wrist design.

B. Wrist Payload

Although the wrist has been serving as a passive joint, FEA analyses have been employed to assess the component's maximum load when subjected to both axial and tangential forces, as illustrated in Figure 13. For instance, utilizing micro servomotors such as the Bluebirds BLS-A930+, which can deliver a maximum torque of 1.94 Nm, we have estimated a maximum load m of 5 kg for the UR joint under axial force mg_A conditions (4 kg under tangential force mg_T conditions) and 3.5 kg for the FE joint under axial force mg_A conditions (2.5 kg under tangential force mg_T conditions). These calculations take into account the use of a flange with a radius of 10 mm. These analyses were carried out by applying the load at a distance of 60 mm from the upper surface of the wrist. Subsequently, the maximum forces F_T that the motors can generate were applied individually to each DOF, and a feasibility analysis was conducted to determine the maximum load that still permits complete deflection θ_{MAX} of each DOF. As for the maximum static load F_L that the component has been capable of enduring in a vertical position with all four motors under tension, a value of 49 kg has been determined.

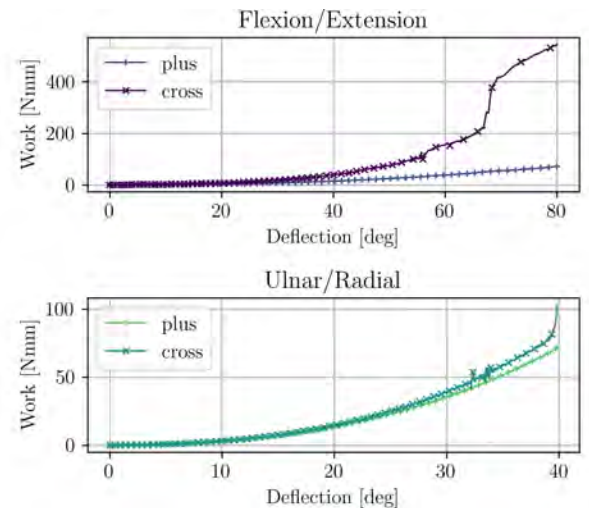


Fig. 12: Comparison of motor work during wrist deflection between 'plus' and 'cross' tendon configurations.

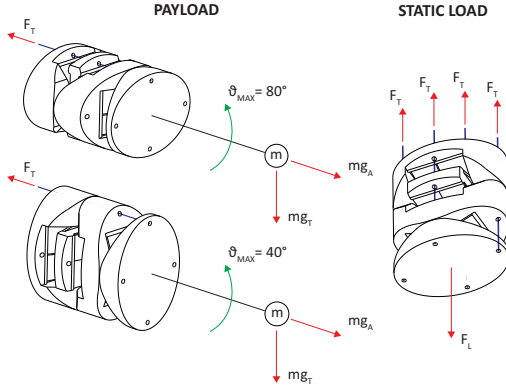


Fig. 13: Payload and Static Load simulation set-up.

This value is comparable to the maximum static load supported by commercially available robotic hands, like the Ottobock Be Bionic hand. In the event of all four motors failing or a complete battery discharge, the joint has demonstrated its capacity to withstand loads of up to 5 kg before reaching the point of failure.

V. EXPERIMENTAL TESTS

To validate the findings of the virtual wrist model, a prototype was produced using Formlabs Fuse and Nylon 11 via Selective Laser Sintering (SLS) technology. Using this SLS technology, the printed piece can achieve remarkable precision (with an average deviation of 0.0395 mm as reported by the manufacturer), eliminating the need for support removal during post-production. Consequently, this approach reduces defects in the slender beams that form the CAFPs. Furthermore, although appropriate tests on physical prototypes are still in the development phase, as reported by Van Hooreweder et al. [29], components manufactured using the SLS technique exhibit a fatigue life comparable to those obtained through injection molding, as well as limited batch-to-batch variability.

Figure 14 displays the physical prototype of the proposed wrist in both its neutral position (picture #1) and maximum deflection angles (i.e. max extension in picture #2, max ulnar deviation in picture #3, and maximum combined extension/ulnar deviation in picture #4). Compared to the one shown in Figure 8, two additional connectors have been included in the model to enable assembly with the experimental test setup. The final device will include either a universal joint or a custom-made one, depending on the prosthetic hand and forearms used. This joint will be attached to the device or produced using additive manufacturing techniques.

The experimental setup illustrated in Figure 15 comprises four Linmot PS01-37x120 linear motors connected to the wrist's four actuation tendons (nylon fishing wire) via axial load cells and pulleys. Closed-loop experimental tests were carried out using a simple PD controller with the help of LabView software, which used the force measurements from the load cells as a reference. Meanwhile, an MPU6050 gyro-accelerometer mounted on the joint's upper surface determined the joint position. A dummy hand was added to the last image of Figure 15 to serve as a reference for the wrist's actual

dimensions. It is important to emphasize that the two DOF within the wrist are mutually independent. For instance, the tendons designed for ulnar/radial deflections do not exert any influence on those designated for flexion/extension deflections. However, due to the dynamic variation in the instantaneous center of rotation of the CAFP joints, shortening one of the two antagonist tendons within a single DOF does not perfectly correspond to the lengthening of its antagonist cable. This distinction necessitates measurement and correction during the experimental tests.

The test setup enabled the collection of data on the actual range of motion (ROM) of the joint, as shown in Figure 16, and the axial forces required for actuation, as presented in Figure 17, and compared to the corresponding values obtained from the virtual prototype in Section III. However, during the combined deflections, the actual ROM was found to be a little lower than the ideal ROM required during the design phase, which may have resulted from suboptimal motor control during the execution of combined FE/UR movements. As future work, an advanced controller capable of fine-tuning the force output of the four motors, taking into account the viscoelasticity of the material, which has been demonstrated to be more accurate in controlling compliant joints [30], will be implemented.

The axial forces required to activate the experimental model also differ from those obtained from FEA simulations. This is because the simulations involve simplifications, such as the absence of friction and actuation only through axial forces at the attachment points of tendons. However, the shapes of the forces are similar. To enhance the accuracy of the virtual model without increasing the computational burden, friction contributions can be estimated using the Euler-Eytelwein formula [31]:

$$F_{f\delta} = F_m e^{\mu\delta} \quad (23)$$

where μ is the Coulomb friction coefficient, F_m is the axial force applied in the virtual model, and δ is the curvature angle for each contact point present in the model. The FEA model can easily measure δ , while μ has been estimated to be 0.25 using the same procedure described in [24]. This simple friction estimation helps the virtual model predict the behavior of the physical prototype more effectively without increasing the computational time of the FEA simulation.

VI. CONCLUSION

This article introduces a novel design of a flexible robotic wrist that has been specifically developed for upper limb prostheses. The wrist incorporates CAFP joints and passive contacts and has been optimized using the Bi-BCM analytical technique. The optimized design has resulted in an exceptional range of motion ($\pm 80^\circ$ FE, $\pm 40^\circ$ UR) that exceeds that of other similar wrists currently available on the market or discussed in the literature. Moreover, the wrist's compact size (measuring 30x40x40(H) mm) and lightweight (20 g) make it an attractive option for prosthetic use.

To validate the analytical optimizer's results and determine the required force for joint activation, Finite Element Analysis

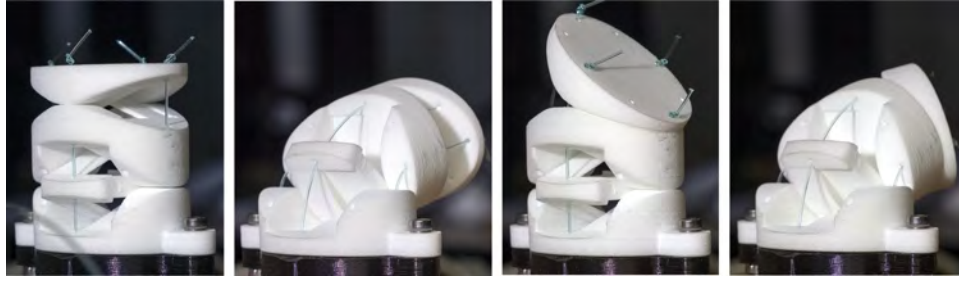


Fig. 14: Physical prototype of the proposed wrist, in his neutral position (picture #1), performing a full extension (picture #2), performing a full ulnar deviation (picture #3) and performing a combined Extension/Ulnar deflection (picture #4).

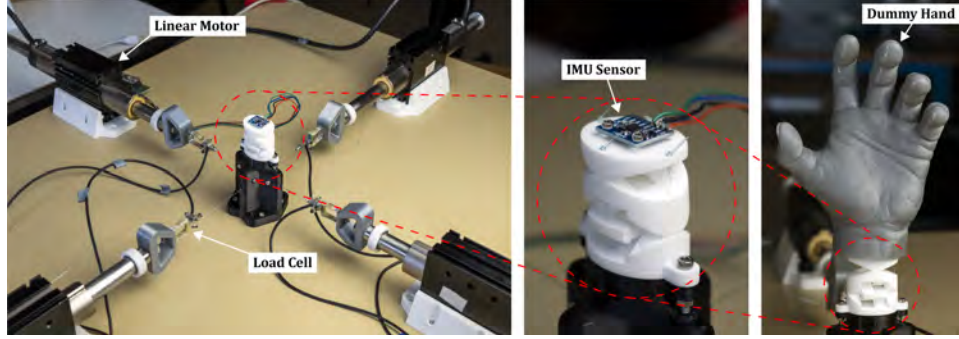


Fig. 15: Experimental setup.

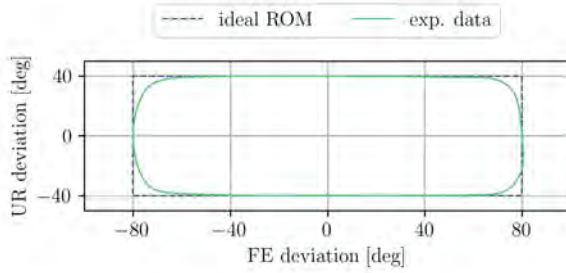


Fig. 16: Wrist range of motion.

tests were conducted. These tests also identified the optimal configuration for positioning tendon channels to minimize prosthesis energy consumption. Experimental tests conducted on the prototype confirmed the actual range of motion and forces generated during wrist movement.

In future work, the wrist will be further evaluated through testing with a robotic hand and forearm. Additionally, a controller capable of considering the viscoelasticity of the flexible components during activation will be developed.

ACKNOWLEDGMENTS

Supported by INTELLIMAN (G.A.No. 101070136), Horizon Europe, Research and Innovation Programme.

REFERENCES

- [1] K. Ziegler-Graham, E. J. MacKenzie, P. L. Ephraim, T. G. Travison, and R. Brookmeyer, "Estimating the prevalence of limb loss in the united states: 2005 to 2050," *Archives of physical medicine and rehabilitation*, vol. 89, no. 3, pp. 422–429, 2008.

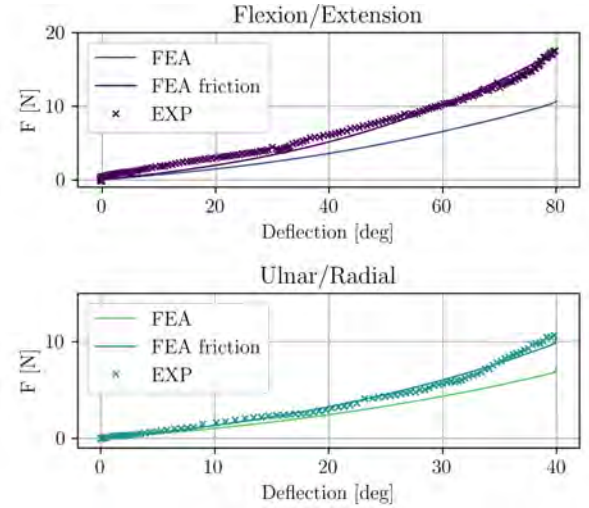


Fig. 17: Reaction forces of the proposed wrist with the maximum allowed deflections, comparison between FEA and experimental tests.

- [2] F. Cordella, A. L. Ciancio, R. Sacchetti, A. Davalli, A. G. Cutti, E. Guglielmelli, and L. Zollo, "Literature review on needs of upper limb prosthesis users," *Frontiers in neuroscience*, vol. 10, p. 209, 2016.
- [3] N. M. Bajaj, A. J. Spiers, and A. M. Dollar, "State of the art in artificial wrists: A review of prosthetic and robotic wrist design," *IEEE Transactions on Robotics*, vol. 35, no. 1, pp. 261–277, 2019.
- [4] G. Lee, G. Y. Hong, and Y. Choi, "Tendon-driven compliant prosthetic wrist consisting of three rows based on the concept of tensegrity structure," *IEEE Robotics and Automation Letters*, vol. 6, no. 2, pp. 3956–3963, 2021.
- [5] A. Demofonti, G. Carpino, N. L. Tagliamonte, G. Baldini, L. Bramato, and L. Zollo, "Design of a modular and compliant wrist module for upper limb prosthetics," *The Anatomical Record*, vol. 306, no. 4, pp. 1–12, 2023.

- 764–776, 2023.
- [6] L. Cappello, D. D'Accolti, M. Gherardini, M. Controzzi, and C. Cipriani, "A 2-degree-of-freedom quasi-passive prosthetic wrist with two levels of compliance," *IEEE Robotics and Automation Letters*, 2022.
 - [7] N. Kim, S. Yun, and D. Shin, "A bioinspired lightweight wrist for high-dof robotic prosthetic arms," *IEEE/ASME Transactions on Mechatronics*, vol. 24, no. 6, pp. 2674–2683, 2019.
 - [8] G. Berselli, A. Guerra, G. Vassura, and A. O. Andrisano, "An engineering method for comparing selectively compliant joints in robotic structures," *IEEE/ASME Transactions on Mechatronics*, vol. 19, no. 6, pp. 1882–1895, 2014.
 - [9] P. Bilancia, M. Baggetta, G. Berselli, L. Bruzzone, and P. Fanghella, "Design of a bio-inspired contact-aided compliant wrist," *Robotics and Computer-Integrated Manufacturing*, vol. 67, p. 102028, 2021.
 - [10] R. W. Schoenmarklin and W. S. Marras, "Dynamic capabilities of the wrist joint in industrial workers," *International Journal of Industrial Ergonomics*, vol. 11, no. 3, pp. 207–224, 1993.
 - [11] D. C. Boone and S. P. Azen, "Normal range of motion of joints in male subjects," *JBJS*, vol. 61, no. 5, pp. 756–759, 1979.
 - [12] T. M. Greiner, "Hand anthropometry of us army personnel," ARMY NATICK RESEARCH DEVELOPMENT AND ENGINEERING CENTER MA, Tech. Rep., 1991.
 - [13] J. W. Garrett, "Anthropometry of the air force female hand," AIR FORCE AEROSPACE MEDICAL RESEARCH LAB WRIGHT-PATTERSON AFB OH, Tech. Rep., 1970.
 - [14] J. Haringx, "The cross-spring pivot as a constructional element," *Flow, Turbulence and Combustion*, vol. 1, pp. 313–332, 1949.
 - [15] B. D. Jensen and L. L. Howell, "The modeling of cross-axis flexural pivots," *Mechanism and machine theory*, vol. 37, no. 5, pp. 461–476, 2002.
 - [16] L. L. Howell, "Compliant mechanisms (2001)," *John Wiley & Sons, Inc*, pp. 1–18.
 - [17] M. Verotti, G. Berselli, L. Bruzzone, M. Baggetta, and P. Fanghella, "Design, simulation and testing of an isotropic compliant mechanism," *Precision Engineering*, vol. 72, pp. 730–737, 2021.
 - [18] F. P. Rad, R. Verthey, G. Berselli, and V. Parenti-Castelli, "Analytical compliance analysis and finite element verification of spherical flexure hinges for spatial compliant mechanisms," *Mechanism and Machine Theory*, vol. 101, pp. 168–180, 2016.
 - [19] J. Dearden, C. Grames, J. Orr, B. D. Jensen, S. P. Magleby, and L. L. Howell, "Cylindrical cross-axis flexural pivots," *Precision Engineering*, vol. 51, pp. 604–613, 2018.
 - [20] S. Hill and S. Canfield, "An assessment of fused deposition modeling for the manufacturing of flexural pivots in an anthropomorphic robotic hand design," in *International Design Engineering Technical Conferences and Computers and Information in Engineering Conference*, vol. 50169. American Society of Mechanical Engineers, 2016, p. V05BT07A066.
 - [21] S. Awtar and S. Sen, "A generalized constraint model for two-dimensional beam flexures: nonlinear load-displacement formulation," 2010.
 - [22] P. Bilancia, G. Berselli, S. Magleby, and L. Howell, "On the modeling of a contact-aided cross-axis flexural pivot," *Mechanism and Machine Theory*, vol. 143, p. 103618, 2020.
 - [23] P. Bilancia and G. Berselli, "An overview of procedures and tools for designing nonstandard beam-based compliant mechanisms," *Computer-Aided Design*, vol. 134, p. 103001, 2021.
 - [24] P. Bilancia, M. Baggetta, G. Hao, and G. Berselli, "A variable section beams based bi-bcm formulation for the kinetostatic analysis of cross-axis flexural pivots," *International Journal of Mechanical Sciences*, vol. 205, p. 106587, 2021.
 - [25] J. Kaufmann, P. Bhovad, and S. Li, "Harnessing the multistability of kresling origami for reconfigurable articulation in soft robotic arms," *Soft Robotics*, vol. 9, no. 2, pp. 212–223, 2022.
 - [26] Z. Chen, B. Tighe, and J. Zhao, "Origami-inspired modules enable a reconfigurable robot with programmable shapes and motions," *IEEE/ASME Transactions on Mechatronics*, vol. 27, no. 4, pp. 2016–2025, 2022.
 - [27] S. Durand, C. P.-Y. Rohan, T. Hamilton, W. Skalli, and H. I. Krebs, "Passive wrist stiffness: the influence of handedness," *IEEE Transactions on Biomedical Engineering*, vol. 66, no. 3, pp. 656–665, 2018.
 - [28] L. Ding, L. Niu, Y. Su, H. Yang, G. Liu, H. Gao, and Z. Deng, "Dynamic finite element modeling and simulation of soft robots," *Chinese Journal of Mechanical Engineering*, vol. 35, no. 1, p. 24, 2022.
 - [29] B. Van Hoorweder, D. Moens, R. Boonen, J.-P. Kruth, and P. Sas, "On the difference in material structure and fatigue properties of nylon specimens produced by injection molding and selective laser sintering," *Polymer Testing*, vol. 32, no. 5, pp. 972–981, 2013.

- [30] M. Baggetta, G. Berselli, G. Palli, and C. Melchiorri, "Design, modeling, and control of a variable stiffness elbow joint," *The International Journal of Advanced Manufacturing Technology*, vol. 122, no. 11–12, pp. 4437–4451, 2022.
- [31] G. Palli, G. Borghesan, and C. Melchiorri, "Modeling, identification, and control of tendon-based actuation systems," *IEEE Transactions on Robotics*, vol. 28, no. 2, pp. 277–290, 2011.

VII. BIOGRAPHY SECTION



Mario Baggetta received his M.S. degree in Mechanical Engineering from the University of Genova in 2019. During his time as a predoctoral Fellow from 2019 to 2020, he was part of the Ansaldo Energia's Lighthouse Plant project. Currently, he is pursuing a Ph.D. degree at the Mechanical Engineering Department of DIME, University of Genova. His research interests include the integrated design of compliant mechanisms, variable stiffness actuators, and collaborative robots. The focus of his doctoral work is on the virtual and physical prototyping of compliant mechanisms and under-actuated robotic hands. He is actively involved in the HE IntelliMan project, which aims to develop an AI-based manipulation system for advanced robotic services, industrial manufacturing, and prosthetics.



Gianluca Palli received the M.Sc. and Ph.D. degrees in automation engineering from the University of Bologna, Bologna, Italy, in 2003 and 2007, respectively. He was a Visiting Student at the Robotic Institute of the German Aerospace Center (DLR), Munich, Germany, in 2006. He is currently Full Professor at the University of Bologna. His research interests include many aspects related to the development of robots able to interact with unstructured environments, deformable objects and to cooperate with humans. He coordinated the WIRES FP7 projects, which aim was to automatize the switchgears wiring process, and he is now the coordinator of the REMODEL H2020 project, aiming at the development of robotic technologies for the manipulation of complex deformable linear objects, and of the HE IntelliMan project, which aims to develop an artificial intelligence-based manipulation system for advanced robotic services, industrial manufacturing and prosthetics.



Claudio Melchiorri is Full Professor in Industrial Robotics at University of Bologna. In the period 2007 - 2013 he was President of the Course of Studies in Automation Engineering at the Faculty of Engineering of the University of Bologna, and in the period 2004-2010 he was Coordinator of the PhD program in "Automation and Operations Research" at DEIS. From 2014 to 2016 he was Coordinator of the PhD program in "Biomedical, Electrical and Systems Engineering" (IBES). He is in charge of the Almatong program, an educational and scientific cooperation with Tongji University, Shanghai, China, where since 2015 he has also held the position of "High End Expert" of the Chinese University Ministry. Since 2014 he has been a member of the Academy of Sciences, Institute of Bologna, and since 2020 he is Fellow of the IEEE.



Giovanni Berselli is Full Professor and Chair of Design Methods for Industrial Engineering at the University of Genova, Italy, where he coordinates the PhD Degree in Mechanical, Energy and Management Engineering. He is also Affiliated Researcher with the Advanced Robotics Department at the Italian Institute of Technology (IIT). Prof. Berselli is currently the Chair of the American Society of Mechanical Engineers (ASME) – Italy Section and the past Chair of the ASME Technical Committee on Modeling, Dynamics, and Control of Adaptive Systems. Prof. Berselli's scientific activity is focused on the design, modelling and experimental evaluation of: i) robot hands and grippers; ii) compliant mechanisms and soft actuators for safe human-robot interaction; iii) energy-aware industrial robotics.